Figure 1.

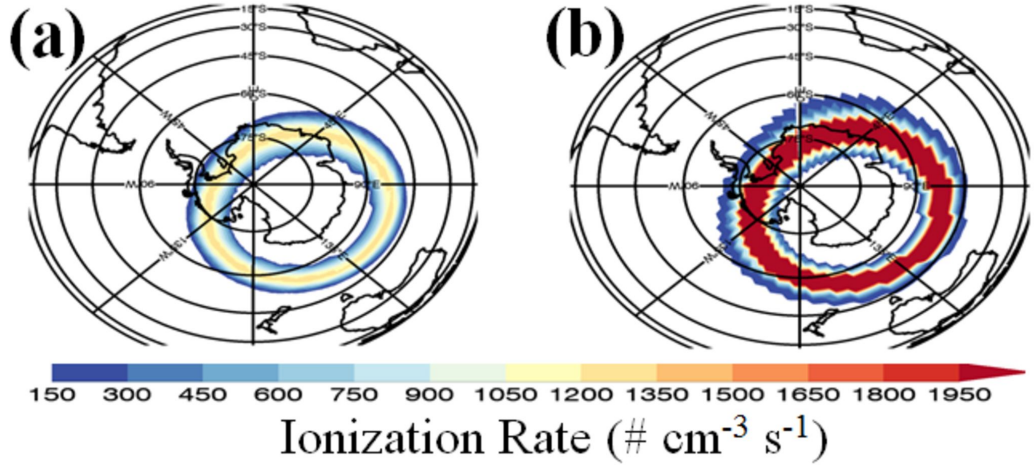
(a)
(b)
150 300 450 600 750 900 1050 1200 1350 1500 1650 1800 1950
Ionization Rate (# cm-3 s-1)

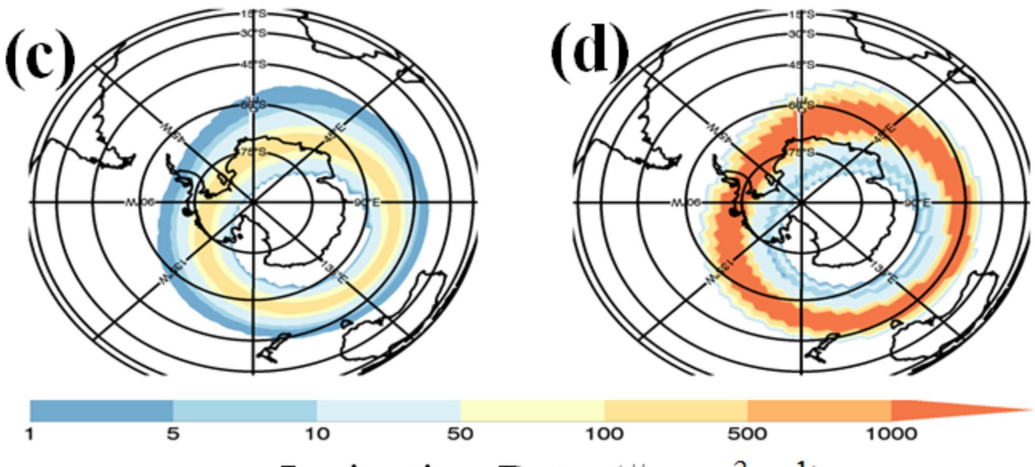
(c)
(d)
1 5 10 50 100 500 1000
Ionization Rate (# cm-3 s-1)

Figure 2.

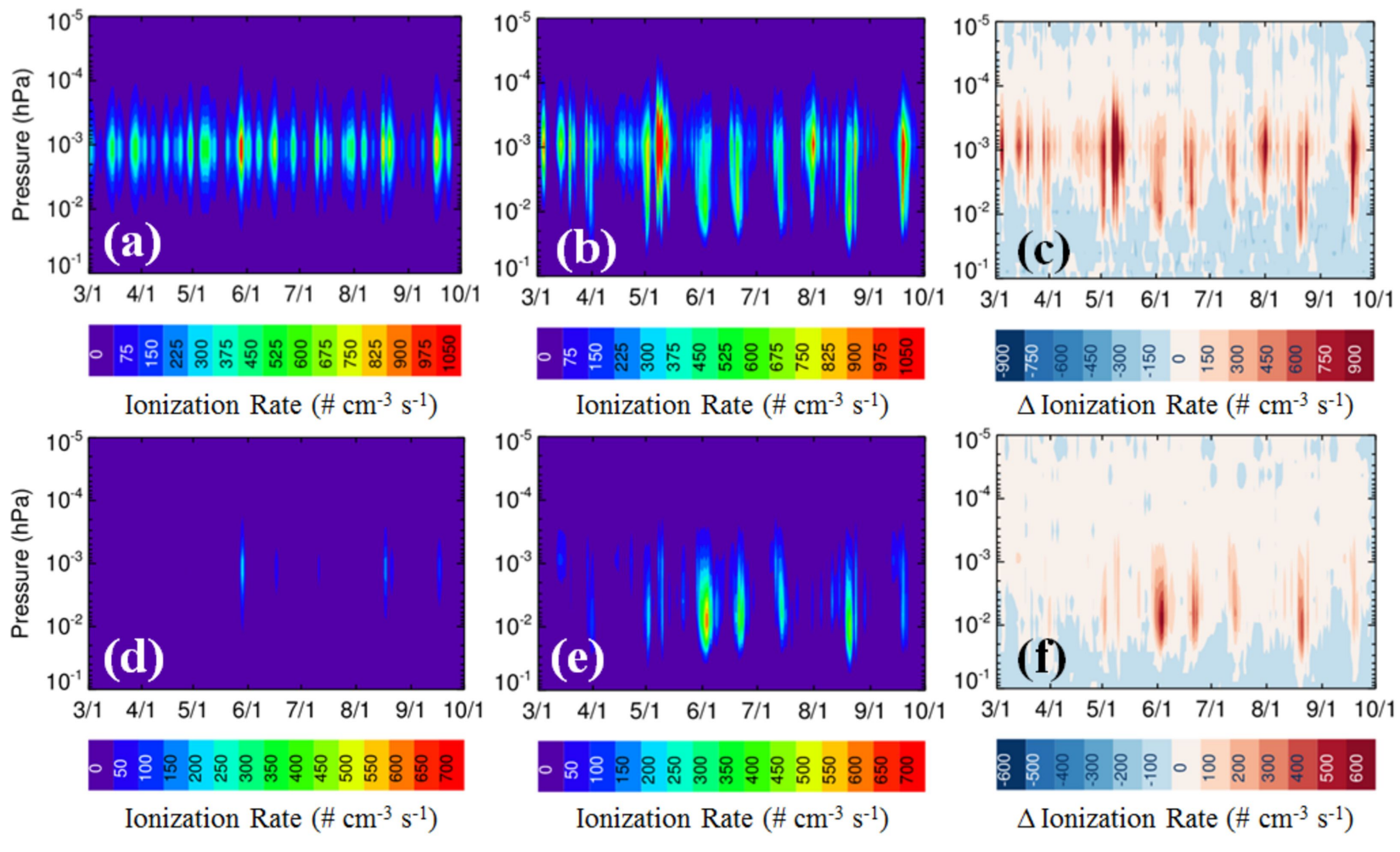
Pressure (hPa)
10^-5
10^-4
10^-3
10^-2
10^-1
(a)
(b)
(c)
(d)
(e)
(f)
3/1 4/1 5/1 6/1 7/1 8/1 9/1 10/1
0 75 150 225 300 375 450 525 600 675 750 825 900 975 1050
-900 -750 -600 -450 -300 -150 0 150 300 450 600 750 900
0 50 100 150 200 250 300 350 400 450 500 550 600 650 700
-600 -500 -400 -300 -200 -100 0 100 200 300 400 500 600
Ionization Rate (# cm-3 s-1)
Δ Ionization Rate (# cm-3 s-1)

Figure 3.

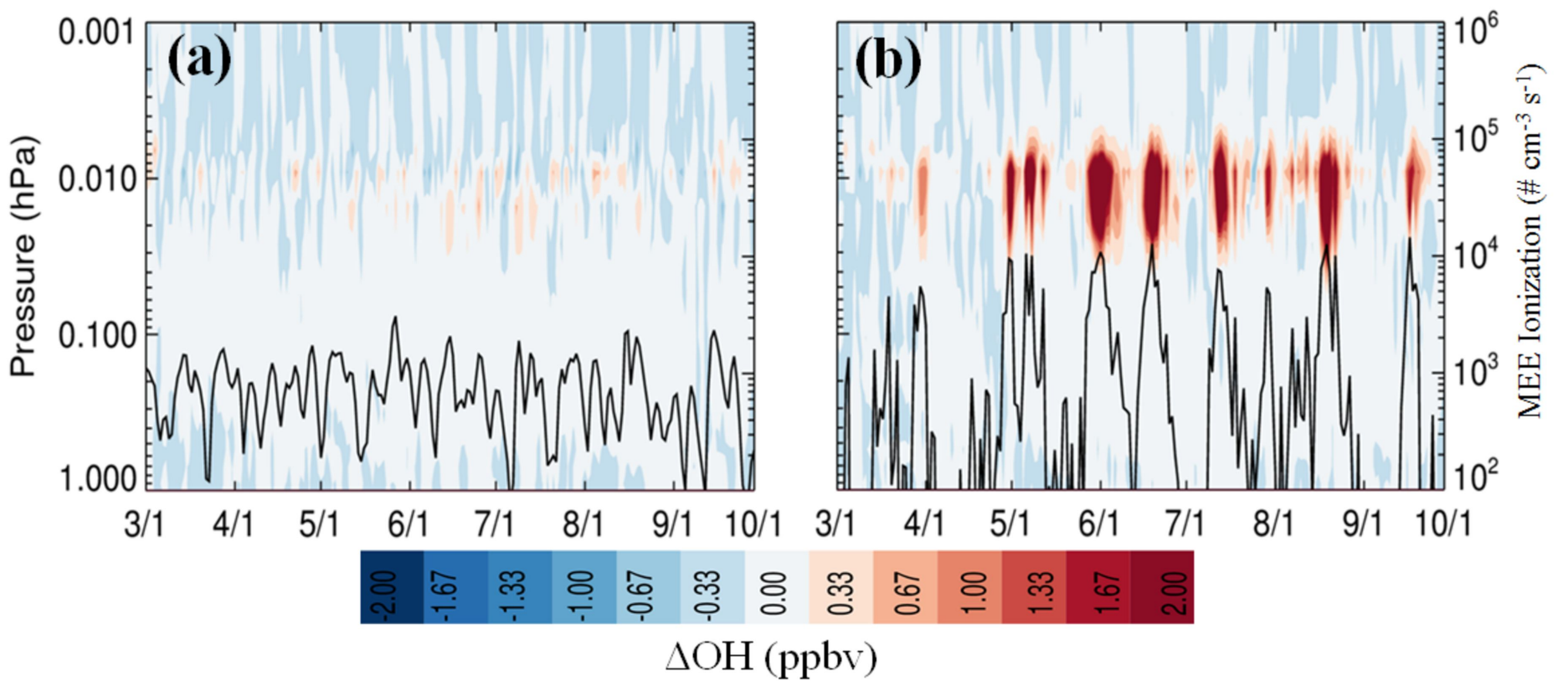
(a)
(b)
Pressure (hPa)
0.001
0.010
0.100
1.000
3/1
4/1
5/1
6/1
7/1
8/1
9/1
10/1
MEE Ionization (# cm-3 s-1)
10^6
10^5
10^4
10^3
10^2
-2.00
-1.67
-1.33
-1.00
-0.67
-0.33
0.00
0.33
0.67
1.00
1.33
1.67
2.00
ΔOH (ppbv)

Figure 4.

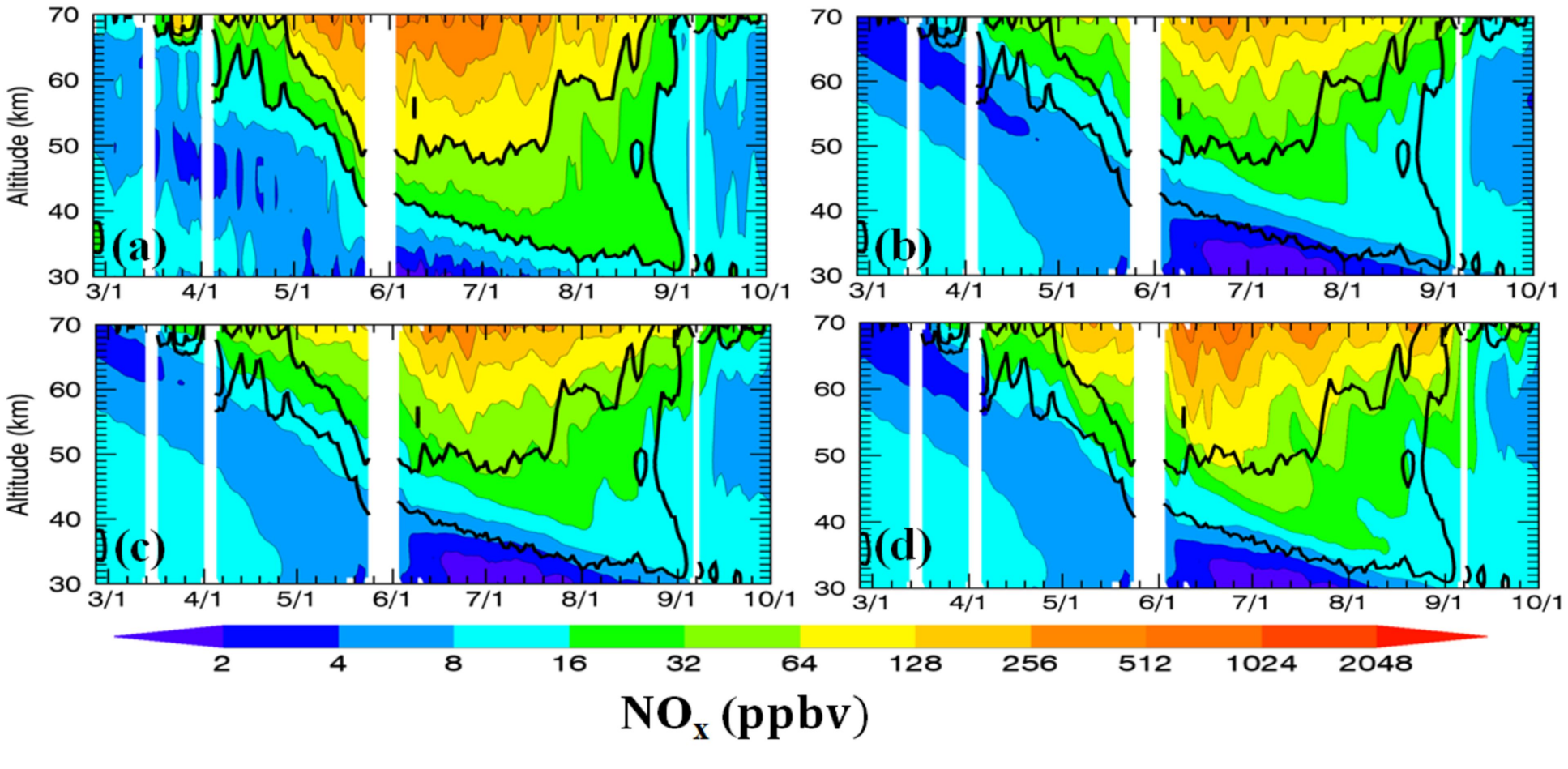
Altitude (km)
70
60
50
40
30
3/1
4/1
5/1
6/1
7/1
8/1
9/1
10/1
(a)
(b)
(c)
(d)
2
4
8
16
32
64
128
256
512
1024
2048
NOx (ppbv)

Figure 5.

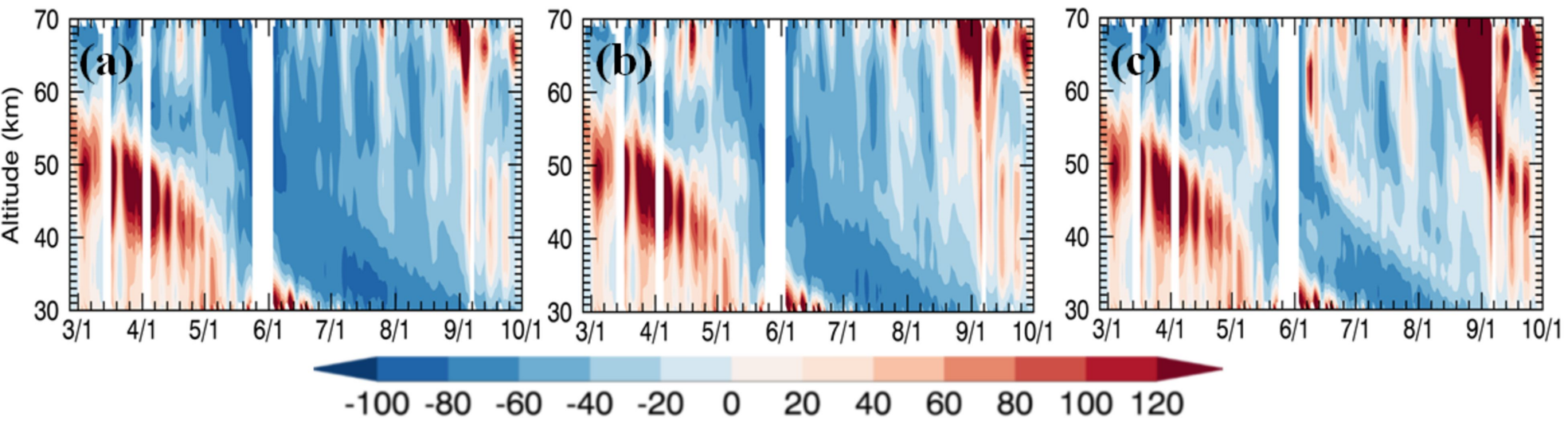
(a)
(b)
(c)
Altitude (km)
70
60
50
40
30
3/1
4/1
5/1
6/1
7/1
8/1
9/1
10/1
-100 -80 -60 -40 -20 0 20 40 60 80 100 120

Figure 6.

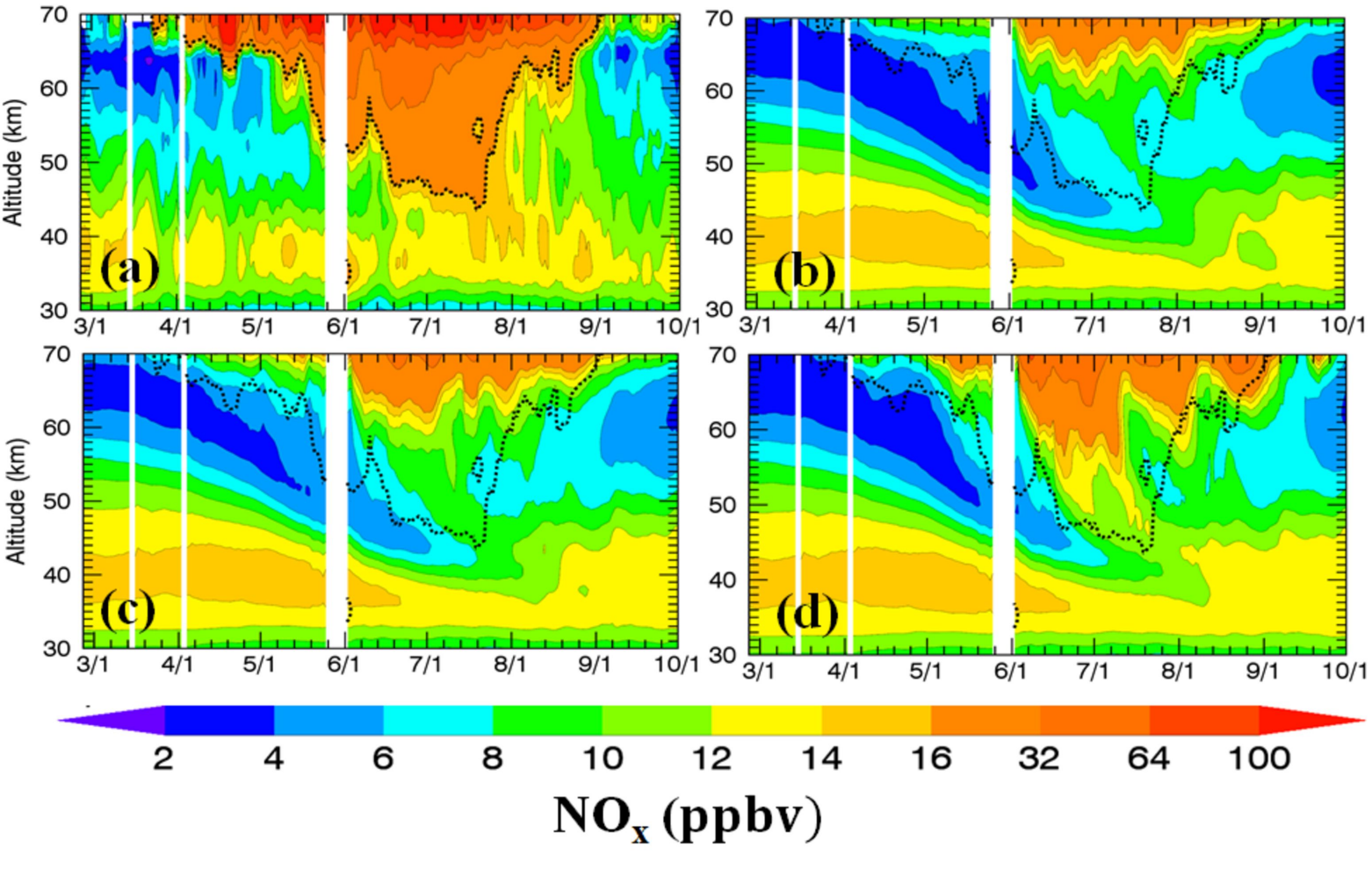
Altitude (km)
70
60
50
40
30
(a)
(b)
(c)
(d)
3/1
4/1
5/1
6/1
7/1
8/1
9/1
10/1
2
4
6
8
10
12
14
16
32
64
100
NOx (ppbv)

Figure 7.

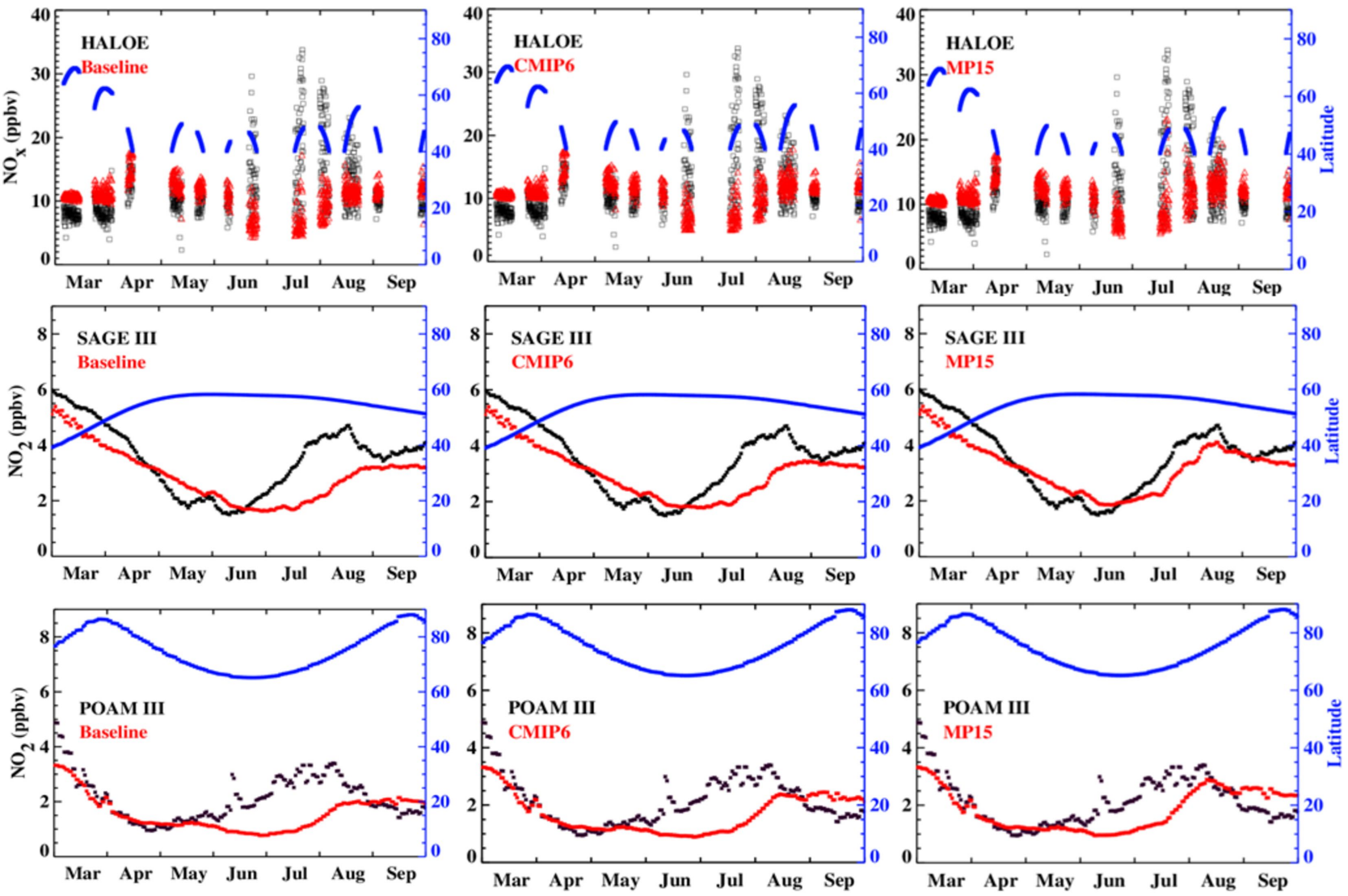
HALOE
Baseline
HALOE
CMIP6
HALOE
MP15
SAGE III
Baseline
SAGE III
CMIP6
SAGE III
MP15
POAM III
Baseline
POAM III
CMIP6
POAM III
MP15
NOx (ppbv)
NO2 (ppbv)
Latitude
Mar
Apr
May
Jun
Jul
Aug
Sep

Figure 8.

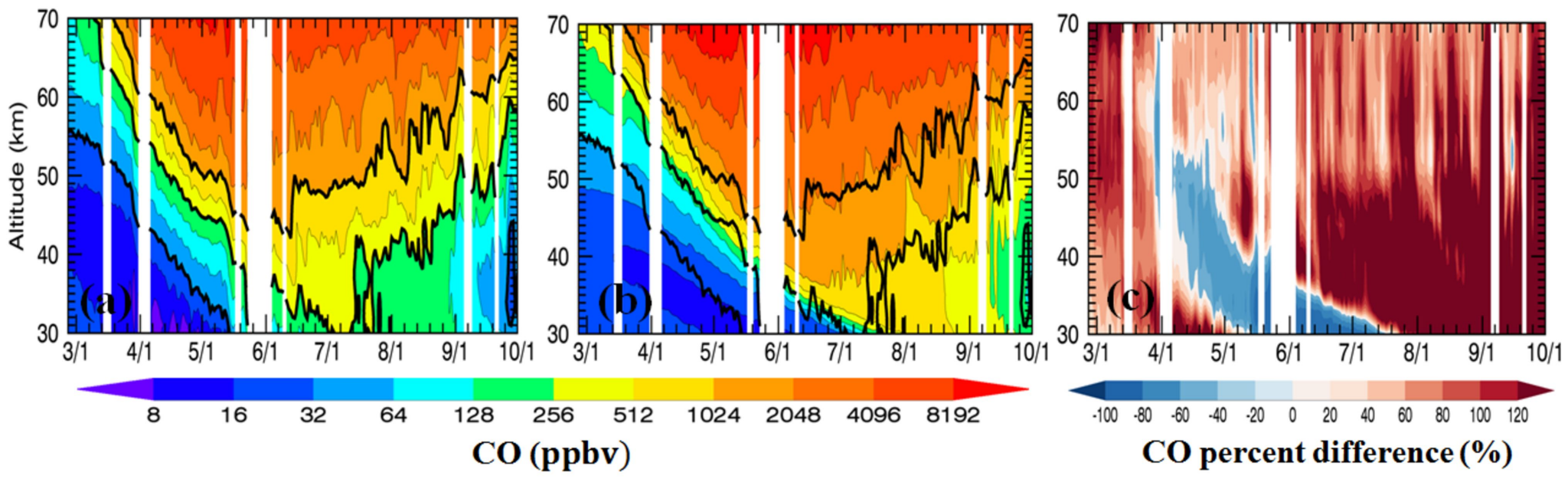
Altitude (km)
70
60
50
40
30
3/1
4/1
5/1
6/1
7/1
8/1
9/1
10/1
(a)
(b)
(c)
8
16
32
64
128
256
512
1024
2048
4096
8192
CO (ppbv)
-100
-80
-60
-40
-20
0
20
40
60
80
100
120
CO percent difference (%)

Atmospheric Effects of >30 keV Energetic Electron Precipitation in the Southern Hemisphere Winter during 2003

J. M. Pettit[1,2], C. E. Randall[1,2], E. D. Peck[3], D. R. Marsh[4], M. van de Kamp[5], X. Fang[1,2], V.L. Harvey[1,2], C. J. Rodger[6], B. Funke[7]

[1] *University of Colorado, Department of Atmospheric and Oceanic Sciences, Boulder, CO,* [2] *University of Colorado, Laboratory for Atmospheric and Space Physics, Boulder, CO, Tamr, Cambridge, MA,* [4] *National Center for Atmospheric Research, Boulder, CO, USA,* [5] *Finnish Meteorological Institute, Helsinki, Finland,* [6] *Department of Physics, University of Otago, Dunedin, New Zealand,* [7] *Instituto de Astrofísica de Andalucía, CSIC, Granada, Spain*

Corresponding author: Joshua Pettit (Joshua.pettit@colorado.edu)

Key Points:

- Effects of energetic electron precipitation in southern hemisphere 2003 simulated with Whole Atmosphere Community Climate Model
- Simulations of middle atmosphere chemistry improve significantly by including > 30 keV precipitating electrons
- Including the full range of pitch angles is necessary to capture precipitating electron impacts at sub polar latitudes

Abstract

The atmospheric effects of precipitating electrons are not fully understood, and uncertainties are large for electrons with energies greater than ~30 keV. These electrons are underrepresented in modeling studies today, primarily because valid measurements of their precipitating spectral energy fluxes are lacking. This paper compares simulations from the Whole Atmosphere Community Climate Model (WACCM) that incorporated two different estimates of precipitating electron fluxes for electrons with energies greater than 30 keV. The estimates are both based on data from the Polar Orbiting Environmental Satellite Medium Energy Proton and Electron Detector (MEPED) instruments, but differ in several significant ways. Most importantly, only one of the estimates includes both the 0° and 90° telescopes from the MEPED instrument. Comparisons are presented between the WACCM results and satellite observations poleward of 30˚S during the austral winter of 2003, a period of significant energetic electron precipitation (EEP). Both of the model simulations forced with precipitating electrons with energies >30 keV match the observed descent of reactive odd nitrogen better than a baseline simulation that included auroral electrons, but no higher energy electrons. However, the simulation that included both telescopes shows substantially better agreement with observations, particularly at mid-latitudes. The results indicate that including energies >30 keV and the full range of pitch angles to calculate precipitating electron fluxes is necessary for improving simulations of the atmospheric effects of EEP.

Plain Language Summary

The study presented here investigates the effects from energetic electron precipitation (EEP) in the southern hemisphere winter of 2003. Electron precipitation is common during periods of enhanced geomagnetic activity and can create reactive nitrogen oxides and hydrogen oxides that can destroy ozone. Most global climate models currently do not include precipitating electrons-with energies greater than 30 keV. To test whether this deficiency is important, this investigation compares observations with model simulations that included electrons with energies greater than 30 keV, as observed by the Medium Energy Proton and Electron Detector (MEPED) satellite instruments. In addition, one of the EEP data sets used in the simulations included data from just one of the telescopes on the MEPED instruments, whereas the other included data from both of the telescopes. We found that including both of the telescopes is important for capturing chemistry changes at polar and sub-polar latitudes. The model simulation that only included only one of the telescopes showed significant improvement compared to a simulation with only low energy electrons. However, it did not perform as well as the model simulation that included both MEPED telescopes. This work is important because it shows that including energies >30 keV and the full range of precipitating electron pitch angles is necessary to show the impact electrons have on the atmosphere and provides an EEP data set for use in future model simulations.

1. Introduction

Space weather's influence on the earth's atmosphere and near-earth environment has attracted significant attention since the satellite era. Solar protons and high-energy electrons can

be very dangerous to astronaut health and can damage expensive space instrumentation (*Parsons and Townsend 2000; Moreno-Villanueva et al., 2017*). In addition, charged particles can enter the atmosphere and disturb the chemistry of the middle and upper atmosphere through energetic particle precipitation (EPP). Atmospheric effects of solar protons and auroral electrons (energy < 30 keV) have been studied extensively over the last few decades (*Jackman et al., 1995; 2004; 2008; 2009; Orsolini et al., 2005; López-Puertas et al., 2005b; Funke et al., 2011; Roble and Rees*, 1977; *Crutzen*, 1979). Particularly in the past several years, more attention has been paid to medium energy electron (MEE; ~30-1000 keV) and high-energy electron (HEE; > 1 MeV) precipitation influences on the atmosphere (*Andersson et al., 2018; Seppälä et al., 2018; Clilverd et al., 2013; Newnham et al., 2018; Verronen et al., 2015*). Evaluating two different energetic electron precipitation (EEP) data sets for inclusion in global climate models, both of which include MEE precipitation inferred from the Medium Energy Proton and Electron Detector (MEPED) instruments, is the focus of this paper. One of the EEP data sets incorporates data from only the 0° MEPED telescope, while the other incorporates data from both the 0° and 90° telescopes.

EEP causes ionization of atmospheric constituents, with electrons of higher energies reaching deeper into the atmosphere. The primary region of energy deposition is ~60-90 km in altitude for MEE precipitation, and lower for HEE precipitation (e.g., *Fang et al.*, 2008, 2010). The ionization leads to significant increases in reactive odd nitrogen (NO_x = N + NO + NO_2) and odd hydrogen (HO_x = H + OH + HO_2) (*Thorne, 1980; Jackman et al., 1980; Solomon et al., 1982; Solomon et al., 1981*). Both of these chemical families are involved in catalytic ozone destruction, making them important for the chemistry and the dynamics of the middle atmosphere. In addition to direct production of NO_x and HO_x by EEP, the indirect effect of EEP (*Randall et al.*, 2006; 2007) also dictates the extent to which EEP affects the middle atmosphere. During the polar winter, when limited light increases the lifetime of the NO_x via photolysis, it descends from the thermosphere and mesosphere into the stratosphere. Furthermore, mesospheric air that was depleted in ozone via EEP-HO_x (*Andersson et al., 2014*) may descend into the stratosphere in the polar winter. In order to simulate accurately the atmospheric effects of EEP, it is important for models to correctly simulate both EEP-induced production of HO_x and NO_x as well as descent rates in the polar winter.

One critical challenge in quantifying EEP effects is determining the spectral energy flux

of electrons that precipitate into the atmosphere (*Clilverd et al., 2010; Rodger et al., 2013; Turner et al., 2012*). Currently, the longest continuous data set of precipitating MEE comes from the observations made by the MEPED instruments onboard the Polar Orbiting Environmental Satellite (POES) constellation, which measure MEE fluxes in the bounce loss cone (e.g., *Rodger et al., 2010*). *Codrescu et al.* (1997) studied the influence of MEE precipitation on the mesosphere and thermosphere using the Thermosphere Ionosphere Mesosphere Electrodynamics General Circulation Model and MEPED data. The simulations showed that MEE precipitation could influence NO_x and HO_x concentrations, leading to ozone depletion in the mesosphere. However, ionization rates used in that study were uncertain since the MEPED electron and proton detectors suffer from multiple issues. Examples are: cross contamination between the electron and proton telescopes (*Asikainen and Mursula*, 2013; *Lam et al., 2010; Rodger et al., 2010; Yando et al., 2011; Peck et al., 2015*), radiation damage to the proton sensors (*Asikainen et al., 2012*), that the telescopes do not sample the entire loss cone (*Rodger et al., 2013*), and that the instruments provide only highly integrated measures of the spectral flux (*Evans and Greer, 2004*). Because of these limitations, and the limited time frame over which MEPED data are available (*van de Kamp et al., 2016*), global climate models have historically excluded MEE and HEE from their specification of EEP, and therefore underestimate the amount of EEP-induced ionization in the atmosphere (e.g., *Randall et al., 2015*). Without accounting for all ionization sources, simulated chemistry changes in the middle atmosphere would be incomplete and underestimated.

Several independent efforts have been made to correct the errors associated with the MEPED instruments, and as a result several corrected electron flux data sets have been created *(Lam et al., 2010; Asikainen and Mursula, 2013; Green et al., 2013; Peck et al., 2015; Nesse-Tyssøy et al., 2016; Asikainen and Ruopsa, 2019).* The study presented here compares results from three different simulations of the National Center for Atmospheric Research (NCAR) Whole Atmosphere Community Climate Model (WACCM), a fully coupled chemistry climate model. All three simulations included auroral electron precipitation, but differed in their inclusion of MEE precipitation. A baseline simulation omitted MEEs. A second simulation specified ion production rates (IPRs) according to the Coupled Model Intercomparison Project version 6 (CMIP6) recommended forcing data set described in *van de Kamp et al.* (2016) and *Matthes et al.* (2017); this data set includes MEE IPRs derived from measurements made by the

0° MEPED telescope. In a third simulation, IPRs for MEE were specified by a modified version of the data set described by *Peck et al*. (2015), which used measurements from both the 0° and 90° MEPED telescopes. Results from all three simulations are compared with each other and with satellite observations for the Southern Hemisphere (SH) winter of 2003.

WACCM is an appropriate model for studying EEP impacts on the atmosphere because the model vertical domain extends to about 140 km. It has been used in previous studies of the atmospheric effects of EEP. *Randall et al*. (2015) showed that WACCM underestimated the amount of NO_x descending to the stratosphere in the Arctic springtime of 2004, attributing the underestimate to a combination of insufficient EEP (only auroral electrons were included in the model used) and inadequate descent rates. *Eyring et al.* (2016) reported the development of a long-term EEP data set for CMIP6 model comparisons, which was derived from the MEPED measurements using the *Ap* magnetic index as a proxy (*van de Kamp et al., 2016*; *Matthes et al*., 2017). *Andersson et al*. (2018) incorporated the CMIP6 EEP data set into a free-running version of WACCM to investigate polar ozone losses from MEE precipitation. They found MEE precipitation to have a significant impact on ozone loss in both the mesosphere and stratosphere. Another recent study used simulations from WACCM-D (WACCM with D-region chemistry) both with and without medium energy electrons as specified by *Nesse Tyssøy et al*. (2016) to simulate the April 2010 EEP event (*Smith-Johnsen et al., 2018*). They found that using D-region chemistry with WACCM improved the direct production of NO versus WACCM without D-region chemistry. Strong correlations between the model and observations were found in the lower thermosphere and in the middle mesosphere; however, near 90-110 km the model underestimated the NO.

The SH winter of 2003 was chosen for the investigation described here for two reasons. First, since the SH shows less variability in polar winter dynamics than the northern hemisphere, simulations of SH winter dynamical conditions are likely to be more robust, facilitating investigations of chemical effects. Second, in May through August of 2003 elevated levels of geomagnetic activity resulted in significant EEP, which makes this an ideal winter for evaluating simulations of EEP effects. The following section discusses the details of the WACCM model and the simulations performed as well as how the EEP data sets are generated. Section 3 describes the results of the simulations and comparisons with observations. Finally, section 4 summarizes and discusses the conclusions of the study.

2. Numerical Simulations and Observations

WACCM is a high-top configuration of the NCAR Community Earth System Model (CESM) (*Hurrell et al., 2013*). The 'high-top' refers to the uppermost level of the atmospheric component, which extends into the thermosphere. WACCM version 4 (*Marsh et al., 2013*) was used in this study, following the protocols defined for the Chemistry-Climate Model Initiative (CCMI, *Eyring et al., 2013*). WACCM4 is based on the Community Atmosphere Model, version 4 (CAM4), and uses a hybrid-sigma coordinate system with 66 pressure levels from the surface extending to 5.1×10^{-6} hPa. The horizontal resolution of WACCM4 is 1.9° lat x 2.5° lon. The chemistry module in WACCM derives from the Model for Ozone and Related Chemical Tracers, version 3 (MOZART3), which is discussed in detail by *Kinnison et al*. (2007), with updates described in *Solomon et al.* (2015). The simulations used in this study applied the 'Specified Dynamics' WACCM (SD-WACCM) mode *(Lamarque et al., 2012; Brakebusch et al., 2013).* SD-WACCM uses reanalysis data from the Modern-Era Retrospective Analysis for Research and Applications (MERRA) *(Rienecker et al., 2011)* to nudge the meteorological conditions in the model to match actual meteorological conditions for the dates of the simulation. That is, at every time step (30-minutes) SD-WACCM calculates new wind and temperature fields by taking 99% of the calculated model data and 1% of the meteorology data. The nudging in this study occurs from the surface to approximately 40 km. The nudging is linearly reduced from 40-50 km, where the model becomes free running (not nudged). SD-WACCM also increases the number of levels from 66 to 88.

To help improve the chemistry in the mesosphere, the D-region chemistry module is adopted in this work, which adds 307 reactions in addition to the default MOZART chemistry (*Verronen et al., 2016*). Many of these reactions are from water cluster ions that are common in the mesosphere. The mesosphere has small quantities of water up through the mesopause. Water cluster chemistry can have a significant impact on odd nitrogen in the mesosphere, but is not included in the default model (*Verronen et al., 2016*). As shown by *Newnham et al.* (2018) and *Smith-Johnsen et al.* (2018), SD-WACCM-D describes the mesosphere and lower thermosphere chemistry during geomagnetically active times more accurately than regular WACCM. For

198 simplicity, for the remainder of the paper we refer to the model used as WACCM, but it should
199 be understood that this is the specified dynamics version of WACCM4 with D-region chemistry.

200 The MEPED instruments (*Evans and Greer, 2004*) used in this study are part of the
201 Space Environment Monitor-2 (SEM-2) platforms that fly aboard POES and the European Space
202 Agency MetOp satellites. The satellites have near circular orbits at about 850 km. Each MEPED
203 instrument consists of two proton telescopes and two electron telescopes. Each telescope pair has
204 a telescope that points 9° away from the zenith ("0°" detector), while the other points 9° away
205 from the anti-ram direction ("90°" detector). Each telescope has a 30° field of view with a
206 combined 2-second sampling time using both detectors. The proton telescopes have 6 broad-
207 band energy channels, labeled P1 to P6 (*Evans and Greer, 2004*). The highest energy channel
208 (P6), which will be discussed more below, measures protons with energies greater than 6.9 MeV.
209 The proton telescopes have cobalt magnets designed to bring incident electrons into an
210 aluminum bin, preventing them from reaching the detector. The electron telescopes have three
211 integrated energy channels, which measure the number of electrons with energies greater than 30
212 keV (labeled E1), 100 keV (E2), and 300 keV (E3). The electron telescopes have a nickel-foil
213 cover to prevent low energy protons from entering the detector. The electrons that reach the
214 detector collide into a silicon sheet that is designed to absorb electrons with energies up to 2.5
215 MeV. Using MEPED data to specify EEP ionization rates requires consideration of several
216 previously documented problems. Cross contamination between the proton and electron
217 detectors causes false detections that must be removed from the electron and proton data (*Lam et*
218 *al., 2010; Green et al., 2013; Rodger et al., 2010; Peck et al., 2015*), and radiation damage has
219 been shown to affect the proton detectors of all POES satellites (*Asikainen and Mursula, 2012).*
220 Radiation damage is one source of error that affects the estimation of proton contamination in
221 electron measurements in both the CMIP6 EPP ionization rates as well as the energetic electron
222 flux data set created according to the method of *Peck et al*. (2015). This source of error can
223 become significant in just a few years after the instrument is launched (*Asikainen and Mursula*
224 *2013; Nesse-Tyssoy et al., 2016*). In addition, the instruments do not sample the entire bounce
225 loss cone (*Rodger et al*., *2013*), so accurately calculating the total precipitating flux requires
226 estimating the MEE pitch angle dependence (*Nesse-Tyssøy et al., 2016).*

The two data sets used in this work, from CMIP6 (*van de Kamp et al*., 2016) and from *Peck et al.* (2015), were chosen because they represent improvements on previous MEPED-based electron precipitation data sets, are publicly available, and are easily incorporated into WACCM. The CMIP6 method of calculating EEP is based on measurements from the 0° MEPED detectors, because the 0° detectors measure electrons within the bounce loss cone, while the 90° detectors measure both trapped and bounce loss cone electrons at middle and high latitudes (*Nesse-Tyssøy et al.,* 2016). The method described in *Lam et al.* (2010) is applied to remove proton contamination from the electron measurements. The corrected electron counts are converted to directional fluxes using the conversion method described in *Evans and Greer* (2004). In cases where the electron directional flux in the E1 channel is less than 250 electrons cm^{-2} sr^{-1} s^{-1}, all channels are set to zero. The corrected directional fluxes are given with 0.5 *L*-shell resolution and one-day temporal resolution across all magnetic local times. To calculate the spectral flux from the three electron channels (E1-E3), a power law spectrum is assumed. As explained in *van de Kamp et al.* (2016), the power law assumption breaks down at energies greater than 1 MeV, so HEE precipitation is not included in the CMIP6 calculations.

After calculating the spectral flux for the time period from 2002-2012 as just described, the data are used to derive a relationship between the fluxes and the *Ap* index for that time period. This relationship is then used to infer the precipitating spectral flux for any given value of the *Ap* index, and these *Ap*-based fluxes are then used to compute vertical profiles of ionization rates via the mono-energetic method of *Fang et al*. (2010). The ionization rate calculations use temperatures and densities from an empirical model of the atmosphere (*Picone et al.,* 2012), rather than the WACCM atmosphere. The resulting data set contains daily ionization rates binned by *L*-shell. An additional step was taken in this study to interpolate the CMIP6 ionization rates to the WACCM grid by converting *L*-shell to magnetic latitude and finally to geographic latitude.

The second EEP data set considered by this study is a modified version of the EEP data set of *Peck et al.* (2015); it is referred to hereinafter as the MP15 data set. Like the CMIP6 calculation, the MP15 data set is also based on POES MEPED data; but there are several notable differences between the CMIP6 and MP15 calculations. The first difference is the incorporation of MEPED measurements from both the 0° and 90° electron detector telescopes, which serves to

broaden the observed pitch angle distribution (*Nesse-Tyssøy et al*., 2016). Based on previous work (e.g., *Gannon et al*., 2007; *Gu et al.*, 2011; *Vampola*, 1998), for MP15 it is assumed that the pitch angle (α) dependence of the precipitating particle flux varies as $\sin^n(\alpha)$, with no particle flux at 0° pitch angle and maximum particle flux at 90° pitch angle. For the MP15 data, n is set equal to 1, since a robust parameterization of the variation with such parameters as magnetic local time and geomagnetic activity is not yet available. Second, to remove proton contamination, inversion methods from *O'Brien and Morley* (2011) were used instead of the method described in *Lam et al.* (2010). Details of the inversion method can be found in *Peck et al.* (2015). Third, since the P6 channel on the proton telescope is intended to record protons with energies >6.9 MeV but also responds to relativistic electrons, in the absence of protons in the P5 channel (which records protons in the range 2.5-6.9 MeV), the P6 channel is a good proxy for highly energetic electrons (*Rodger et al. 2010*). Therefore, *Peck et al*. (2015) use the P6 channel to create an additional virtual electron channel (E4) that quantifies electrons with energies (>1 MeV). Thus all four channels (E1-E3 plus E4) are used in the calculation of MP15 differential flux values, and the energetic electron flux spectra extend to 10 MeV instead of 1 MeV. Fourth, rather than assuming that the differential electron flux follows a power law, *Peck et al*. (2015) fit a combined spectrum of a relativistic Maxwellian, double Maxwellian, power law, and energy exponential to the MEPED electron channel measurements.

Three improvements to the method of *Peck et al*. (2015) are included for our current investigation. *Peck et al*. (2015) included electron counts in all *L*-shells from the MEPED detectors. However, at very low geomagnetic latitudes MEPED is sensitive to both drift cone and trapped electrons as well as to bounce loss cone electrons. The majority of the electrons that exist at *L*-shells less than 2 are most likely trapped electrons that will not precipitate into the atmosphere (*Rodger et al., 2013*). Therefore, to improve the MEPED data set for this investigation, any electron counts below *L*-shell 2 were removed prior to processing the data. In addition, to be consistent with the CMIP6 data set, electron counts from *L*-shells larger than 10 were also removed. Lastly, after converting count rates to directional fluxes, those measurements with fewer than 250 electrons cm^{-2} sr^{-1} s^{-1} were removed from the data set, since this is close to the noise floor of the MEPED instruments; this is in agreement with the CMIP6 method (*van de Kamp et al., 2016*).

In addition to the differences in electron flux calculations, the CMIP6 and MP15 simulations also differ in their approach for undertaking ionization rate calculations. Instead of calculating ionization rates offline using a separate atmospheric model as in the CMIP6 simulation, for the MP15 simulation the electron flux spectra are interpolated from the original MEPED measurement locations to the WACCM grid points. In order to include enough observations to create a robust map, each daily map on the WACCM grid includes five days of MP15 electron flux spectra, centered on the day of interest. This does bring small errors into the calculation because the five day averaging causes some artificially elevated ionization rates prior to stronger events. The results are hemispheric maps of electron flux spectra that are used as input to WACCM, and ionization rates are computed self-consistently within WACCM using the model temperatures and densities, following *Fang et al.* (2010). Since ionization rates based on *Fang et al.* (2010) have not yet been validated for electrons greater than 1 MeV, fluxes in energy bins higher than 1 MeV were removed before calculating ionization rates. Thus neither the CMIP6 nor the MP15 EEP data sets include HEE precipitation. The MP15 maps allow for 3D ionization rate profiles, as compared to the CMIP6 data, which are zonally averaged on each L-shell.

WACCM results are compared with several different satellite instrument observations. The Michelson Interferometer for Passive Atmospheric Sounding (MIPAS; *Fischer et al*., 2008) was operational from 2002-2012 and measured several minor atmospheric constituents as well as temperature using atmospheric limb emissions from 4.15 μm to 14.6 μm. As an infrared emission instrument, MIPAS sampled globally each day. This study uses NO_x ($NO+NO_2$) from the MIPAS version V5H data set (*Funke et al.*, 2014). For the time period of interest here, NO_x is available at altitudes from the clouds' top to 72 km, with a vertical resolution of 3 km in the stratosphere and 5-10 km in the mesosphere. The Halogen Occultation Experiment (HALOE; *Russell et al*., 1993) is one of four solar occultation instruments used in this study. It measured temperature and several trace gases including NO and NO_2 from 1991-2005. Like other solar occultation instruments in low earth orbit, it provided ~15 vertical profiles around two different latitude circles on any given day, at spacecraft sunrise and sunset. HALOE Version 19 NO_x data is used here (*Gordley et al.*, 1996; see also *Randall et al*., 2002). The second solar occultation instrument employed is the Polar Ozone and Aerosol Measurement (POAM) III. POAM III measured vertical profiles of NO_2 between 20 and 60 km, from 1998-2005. The POAM NO_2 data

used here is version 6.0 (*Randall et al*., 2002), which has a vertical resolution of 1-2 km between 22 km and 37 km in altitude, increasing to 3 km near 40 km and 7 km at 45 km. The third solar occultation instrument is the Stratospheric Aerosol and Gas Experiment (SAGE) III on the Meteor-3M spacecraft, which operated from 2002-2005. SAGE III measured ozone, aerosols and NO_2 density profiles from cloud top to 40 km with a vertical resolution of 1 km (*Rault et al.,* 2004). The SAGE III NO_2 data product version 3.0 is utilized here.

The three simulations conducted for this investigation are referred to as the baseline, CMIP6, and MP15 simulations. The baseline simulation included auroral electrons, but no MEE or HEE. The CMIP6 simulation included the CMIP6 MEE ionization rates, and the MP15 simulation used spectral fluxes as described above, with ionization rates calculated inline in WACCM. All model simulations were run from January through September 2003 and were forced with daily aurora input based on the parameterized auroral oval of *Roble and Ridley* (1987). All three simulations included ionization from solar protons. Input values of proton fluxes for the solar proton events (SPEs) were taken from GOES measurements. A detailed description of how the proton fluxes are input into the model is available in *Vitt and Jackman* (1996). In previous work, hourly proton fluxes were binned into daily averages before the ion production rates were calculated (*Jackman et al., 2008; 2009*). In the simulations presented here, the ion production rates from SPEs were hourly, not daily. During the SH winter of 2003, there were very minor SPEs on 29 May, 31 May, and 19 June, but no major events.

3. Results and Discussion

Figure 1 gives a snapshot of the ion production rates from the CMIP6 and MP15 data sets on two days in May of 2003 at altitudes of 90 km and 75 km. This was during a period of enhanced geomagnetic activity. Both simulations show a similar geographic distribution at these altitudes, with a displacement toward Australia due to the location of the magnetic pole. However, peak ionization rates in the MP15 case are more than a factor of three higher than in the CMIP6 calculation at 90 km. At the lower, 75 km, the MP15 shows higher ionization rates as well and the peak ionization rates are geographically different between the two data sets. Particularly noteworthy is the extension of high ionization rates to more equatorward latitudes in

MP15 than in CMIP6 at lower altitudes; this has an important effect on the model results, and will be discussed more below.

Figure 2 shows a time series of the ionization rate vertical profiles from the CMIP6 and MP15 data sets during the SH winter from March through September 2003. The rates are averaged from 50°S to 80°S geographic latitude in Figure 2a and 2b, and averaged from 30°S to 50°S in Figure 2d and 2e. The differences between the two are shown in Figure 2c and 2f (MP15-CMIP6). At high latitudes, the timing of ionization events is similar in both data sets, although there are some differences that we attribute to the fact that the CMIP6 data set is parameterized according to the *Ap* index, so it does not necessarily reproduce the MEPED variations precisely. As noted by *van de Kamp et al.* (2016), errors associated with the CMIP6 EEP ionization rates can reach a factor of 10. It is clear from the figure that overall the MP15 ionization rates are larger than the CMIP6 rates, and that the MP15 ionization extends to lower altitudes, as quantified in panels c and f. The CMIP6 simulation resulted in very little ionization at 30°S-50°S (panel d), whereas the MP15 simulation shows significant ionization at these latitudes during geomagnetically active time periods. The larger rates are primarily due to the MP15 use of both the 0° and 90° MEPED telescopes, which extends the latitude extent farther equatorward than using just the 0° telescope. Another interesting feature is the difference in altitudes where the peak ionization occurs. The peak CMIP6 ionization rates occur at nearly the same altitude during all periods, whereas the MP15 peak ionization altitude varies with the event, often peaking at lower altitudes than in CMIP6. For example, the altitude of the MP15 peak ionization on 1 August is at 0.001 hPa (~96 km), while the 1 June peak is near a pressure level of 0.01 hPa (~80 km). This is likely due mainly to the inclusion of the 90° detector, which tends to have higher energy electrons than the 0° detector and to a lesser extent differences in the calculation of spectral fits to the MEPED electron channel data. As mentioned in the previous section, the MP15 spectral flux calculation uses a combination of analytical functions to fit the MEPED integrated electron flux measurements. Although the ionization rate calculations include only the fluxes of electrons with energies less than 1 MeV, the multi-function fit is applied to MEPED data that extends to 10 MeV. The CMIP6 spectral flux calculation, on the other hand, uses a power law fit that includes only energies up to 1 MeV. Both the functional form and the inclusion of higher energy electrons will cause MP15 spectral fluxes to exceed those of CMIP6 for the highest energy electrons (e.g., 300 keV – 1 MeV), which precipitate at the lower altitudes.

To show the impact of MEE precipitation on OH, Figure 3 shows OH mixing ratio differences between the baseline simulation and the model simulations that were forced with the CMIP6 (Figure 3a) and MP15 (Figure 3b) data sets. The plots show the differences as forced minus baseline; for brevity, we refer to the simulations that include MEE ionization as "forced", but it should be understood that even the baseline simulation includes auroral electrons and SPEs. Results were averaged over latitudes from 50°S-80°S and are shown for the months of March through September. Over-plotted on each panel are the MEE ionization rates at 0.01 hPa from the respective simulations. We chose to show this altitude because this is where the largest change in OH is seen. Tick marks on the horizontal axes denote the first day of each month. The CMIP6 simulation shows relatively little OH increase from MEE precipitation, whereas the MP15 simulation shows large increases during periods of electron precipitation. The black lines indicate that the timing of the OH increases coincided with MEE ionization. OH increases of at least 2 ppbv can be seen during periods of elevated EEP in the MP15 simulation. The odd hydrogen lifetime in the mesosphere is on the order of hours (*Solomon et al*., 1983), so as expected, Figure 3 shows no evidence of the OH being transported to lower altitudes. The MP15 simulation did show some moderate ozone loss in the SH polar mesosphere from the OH production during this time period (not shown); ozone mixing ratio losses of 0.5 - 0.75 ppmv were found at 0.05 hPa, and coincided with the altitudes and times of OH increases.

Figure 4 shows NO_x mixing ratios from the MIPAS instrument (a), the baseline simulation (b), the CMIP6 simulation (c), and the MP15 simulation (d), during the SH 2003 winter. All panels show averages between 70°S and 90°S, and the model was sampled at the satellite observation times and locations. The model results were interpolated to an altitude grid with a 1 km vertical resolution using model geopotential height. The black contours are included for guidance, and denote the 16 ppbv and 64 ppbv levels from the MIPAS data. Areas of white in Figure 4a indicate either missing MIPAS data (so these areas are also shown as white in the numerical simulations), or MIPAS data with errors greater than 200%. All simulations show a "tongue" of descending NO_x throughout the winter, as expected from the observations. This is unambiguously identified as EPP-NO_x, since EPP is the only source of NO_x in the mesosphere and lower thermosphere (MLT) during the polar winter. It is clear, however, that both the baseline and the CMIP6 simulations underestimate the descending NO_x mixing ratios relative to MIPAS, with the low bias apparent all the way up to 70 km. In combination with the fact that the

CMIP6 simulation agrees slightly better with MIPAS than the baseline, this suggests that the underestimate is caused at least partially by too little production of EPP-NO_x, although too little descent in the MLT could also contribute. More EPP-NO_x is produced in the mesosphere in the MP15 simulation because of the higher ionization rates, so the MP15 simulation more accurately matches the observations. Even in the MP15 simulation, however, WACCM often shows a NO_x deficit in the tongue, indicating that too little EPP-NO_x descended into the stratosphere. That this most likely results from insufficient descent rates is supported below by an analysis of WACCM carbon monoxide (CO), which serves as a tracer of vertical transport.

To quantify the differences between the forced simulations and the observations, the percent differences in NO_x mixing ratios between the WACCM simulations and the MIPAS measurements are presented in Figure 5. Areas of blue show where WACCM underestimates NO_x relative to MIPAS, whereas red regions indicate overestimations. The CMIP6 simulation (Figure 5b) is a significant improvement over the baseline simulation (Figure 5a), but results show a systematic NO_x deficit of 20% – 80% relative to MIPAS at most altitudes in May through August. During this same time period, differences between the MP15 simulation and MIPAS are more often within ±40%, consistent with the qualitative conclusion from Figure 4 that the MP15 simulation more accurately reproduces the tongue of descending EPP-NO_x. However, Figure 5 also shows large regions where all three simulations overestimate NO_x compared to MIPAS. This is particularly evident below 60 km in March and April, and above 40 km in late August and September. The former is attributed to a high NO_x bias in the initial model conditions that descends with time as air is transported downward by the residual circulation. The latter appears to reflect a high bias in the amount of descending EPP-NO_x above the top altitude of the MIPAS measurements, which then descends with time from 60-70 km in late August into the stratosphere in September. This bias could be caused by too much production of NO_x via EEP (EEP-NO_x) and/or too-rapid descent in the mesosphere and lower thermosphere (MLT), but no measurements are available to definitively distinguish between these possibilities. The high bias in late August and September is largest in MP15, followed by CMIP6 and then the baseline simulation, which suggests that the different MEE flux estimates contribute to the bias. That even the baseline simulation shows a high bias would argue that too much auroral EEP and/or too-rapid descent in the MLT also contributes to the bias. An overestimate of auroral EEP is consistent with the WACCM results for the northern hemisphere winter of 2004 reported by

Randall et al. (2015), but inconsistent with the WACCM simulations of a geomagnetic storm in April 2010 reported by *Smith-Johnsen et al*. (2018). The possibility that the bias is caused by too-rapid (or prolonged) descent is revisited below in the discussion of Figure 8.

As discussed above, incorporating data from both the 0° and 90° MEPED telescopes in the MP15 data set results in more EEP-NO_x production at mid-latitudes than in the CMIP6 simulation. To investigate the mid-latitude effects further, Figure 6 compares MIPAS NO_x observations with the model results for latitudes between 40°S and 50°S. The dashed black line denotes the 16 ppbv NO_x contour from the MIPAS observations, and is included for guidance. The MIPAS data show clear evidence of EEP-NO_x descending from the mesosphere into the stratosphere at mid-latitudes during the SH winter. The CMIP6 simulation shows very little descending EEP-NO_x, because electron ionization using only the 0° detector would be confined primarily to more polar latitudes. The MP15 simulation more closely matches the observations, but does underestimate NO_x mixing ratios in the stratosphere and mesosphere. This could indicate too little ionization at these latitudes and altitudes, and/or that there are errors in the meridional and/or vertical transport. Nevertheless, Figure 6 confirms that including the 90° telescope, and possibly better constraining the spectral distribution for energies of 300 keV – 1 MeV, improves simulation results significantly for the mid-latitudes.

To broaden the comparisons to other available measurements, Figure 7 compares observations of NO_x at 45 km altitude from HALOE (top row), and of NO_2 at 40 km altitude from SAGE III (middle) and POAM III (bottom, all in black), with WACCM results at the corresponding locations and times from the baseline (left), CMIP6 (middle) and MP15 (right) simulations (all in red). The latitudes of the measurements are plotted in blue and referenced to the right vertical axis. In March to September of 2003, HALOE measurement locations swept rapidly through sunlit latitudes between 69°S and 77°N, resulting in observations that were only occasionally at SH latitudes influenced significantly by MEE precipitation. Figure 7 shows all HALOE SH measurements poleward of 40°S, since these are the latitudes most relevant to the current investigation. Note that most of these measurements were between 40°S and 50°S, with excursions to polar latitudes in March and early April, and an excursion to 56°S in August. As might be expected for an altitude of 45 km at mid-latitudes, there is little difference between the baseline and CMIP6 simulations, since neither includes ionization from electrons at these

latitudes. All three simulations overestimate NO_x mixing ratios at 40 km in March through May, reflecting a high bias that was present at the beginning of the simulations. But by late June, when the HALOE data exhibit a substantial enhancement due to descending EPP-NO_x, all three simulations underestimate the observed NO_x. This is consistent with the mid-latitude MIPAS results in Figure 6, and with the early deficit in simulated descending NO_x at polar latitudes shown in Figures 4 and 5. Nevertheless, the MP15 simulation, which includes electron flux at lower latitudes, more closely matches the HALOE NO_x mixing ratios from mid-July through August, once again highlighting the need to include count rates from the 90° telescope in electron flux calculations.

Moving to slightly more polar latitudes, the middle row of Figure 7 shows comparisons between the WACCM simulations and SAGE III measurements at 40 km. Since the SAGE III measurement latitudes changed slowly with time, Figure 7 shows seven-day running averages of the measurements. Only NO_2, not NO_x, is shown, because SAGE III did not measure NO. One can infer from the MIPAS data in Figures 4 and 6 that the increase in NO_2 mixing ratios observed by SAGE III in late June and July was caused by descent of EEP-NO_x to 40 km. The subsequent decline in August most likely indicates that the tongue of NO_x-rich air had descended below 40 km, so NO_2 at 40 km was returning to background levels at this time. Both the CMIP6 and baseline simulations show a deficit of NO_2 from July through September, with maximum differences of about 2 ppbv, or 50% of the observed NO_2. The MP15 simulation, however, compares very well with SAGE III. The improved agreement is again attributed to the fact that MP15 includes electron precipitation outside the polar region, which is influential at the latitudes sampled by SAGE III. Thus, in agreement with the mid-latitude MIPAS and HALOE comparisons, the SAGE III comparison confirms that including measurements from both MEPED telescopes in electron flux calculations is important for accurate simulation of EEP effects at mid latitudes.

As shown by the bottom row in Figure 7, POAM III sampled latitudes poleward of 60°S throughout the March to September time period. Like SAGE, POAM measurement latitudes changed slowly with time, so Figure 7 shows seven-day running averages of the measurements; also like SAGE, POAM measured NO_2, but not NO. The MIPAS data in Figure 4 indicate that 40 km was near the lower edge of the tongue of descending polar NO_x in June and July, well

within the tongue throughout most of August, and above the tongue in September. Thus, as in the SAGE observations, the increase in POAM NO_2 mixing ratios in June and July is indicative of the descent of EEP-NO_x from higher altitudes down to 40 km. The decline in August-September is attributed mostly to the fact that, as noted above, the tongue of EEP-NO_x descended below 40 km in September, so polar NO_x mixing ratios at 40 km were declining to their background values at this time. There might also be a contribution from the change in latitude of the POAM measurement sampling, from ~71°S in early August to 88°S on 22 September. MIPAS data confirm that NO_2 mixing ratios at 40 km decreased slightly toward the pole in September (not shown), so it is expected that the POAM sampling excursion would result in a decline in NO_2.

Consistent with the MIPAS NO_x comparisons from 70°S-90°S in Figures 4 and 5, all of the WACCM simulations underestimate the increase at the POAM measurement locations in June and July, but the MP15 simulation comes closest to reproducing it. Maximum NO_2 mixing ratios of 3.5 ppbv were measured by POAM in early August, and only the MP15 simulation shows values up to 3 ppbv; maximum mixing ratios in the baseline and CMIP6 simulations are only ~2 and 2.5 ppbv, respectively. It thus appears that the amount of EEP-NO_x that descends to 40 km in the MP15 simulation is sufficient, but that the timing is delayed, possibly because of too little descent to 40 km in June and early July. As noted above, POAM NO_2 mixing ratios declined in August-September to less than 2 ppbv, whereas the NO_2 mixing ratios in all three simulations remain relatively constant (baseline and CMIP6) or decline just slightly (MP15) after reaching their maximum values. That all of the simulations show too little decrease in 40-km NO_x mixing ratios in September suggests that the cause is most likely unrelated to the EEP specification, and is more likely due to errors in MERRA-forced WACCM transport caused either by too much replenishment, or too little removal, of NO_x-rich air at 40 km at the POAM measurement locations. As noted above, the MIPAS comparisons in Figures 4 and 5 suggest that there is too much descent of NO_x-rich air from the mesosphere into the stratosphere in late August and September in the WACCM simulations.

To evaluate vertical transport in WACCM, simulated CO was compared with MIPAS CO, since CO is a tracer that can be used as a proxy for descent in the mesosphere and upper stratosphere during the winter (*Allen et al*., 1999; *Harvey et al*., 2015). Figure 8 shows CO mixing ratios from MIPAS (a) and WACCM (b), and the percent differences (c), averaged over

70°S-90°S in March through September of 2003. Results from only the baseline simulation are shown; but as expected, CO mixing ratios are similar in all three simulations. The black contour lines are guides that denote the 32 ppbv, 256 ppbv, and 1024 ppbv contour lines from MIPAS. Qualitatively, the WACCM and MIPAS CO mixing ratios are morphologically similar. Except for a week in early May, however, the MIPAS CO contours in March through early June are steeper than the WACCM CO contours, which indicates that WACCM descent is too slow at this time. While this should lead to negative differences between WACCM and MIPAS, the systematic high bias in WACCM at the beginning of the time series leads to the positive differences in Figure 8c throughout March at most altitudes, and also in April through June at sequentially lower altitudes as the CO at 70 km and above descends with time. In April and May below 60 km, the vertical gradient in CO steepens in WACCM (i.e., the color contours in Figure 8b become compressed), because simulated descent rates at the lower altitudes decrease relative to those at the higher altitudes. This does not appear to occur in the observations (Figure 8a). In addition, the MIPAS data indicate strong downwelling below 50 km in mid-May that is not captured in the simulation. Together, these differences lead to the swath of negative differences in Figure 8c that begins in late March and descends with time through June. Descent rates above 40 km from mid-June through September cannot be inferred from Figure 8; but a continued underestimate of descent rates early in the winter would be consistent with the early winter NO_x deficits discussed above. WACCM CO mixing ratios in August and September are higher than MIPAS mixing ratios throughout the polar stratosphere, which appears from Figure 8b to result from too much CO descent. If this is indeed indicative of descent that is too prolonged in WACCM, it could explain the high bias in NO_x mixing ratios in the MP15 simulation in September, and the lack of NO_2 decline at 40 km in the comparisons in Figure 7.

4. Conclusions

This work compares SD-WACCM simulations of the 2003 SH winter using two different estimates of MEE ionization rates. In the "CMIP6" SD-WACCM simulation, the publicly available CMIP6 EEP ionization rates (*Eyring et al*., 2016) were prescribed. The CMIP6 ionization rates are derived from an Ap-index-based parameterization of measurements from the MEPED 0° electron detector telescope (*van de Kamp et al*., 2016). In the "MP15" SD-WACCM

simulation, MEE spectral fluxes from an improved version of the MEE data set described by *Peck et al.* (2015) were input to SD-WACCM, and ionization rates were calculated within SD-WACCM. The MP15 electron fluxes are based on measurements from both the MEPED 0° and 90° electron detector telescopes. Both the CMIP6 and MP15 SD-WACCM simulations included precipitating electron energies up to 1 MeV. However, the analytical fits used to convert spectrally integrated MEPED electron fluxes to differential spectral fluxes used different functional forms, and the MP15 fits extended to energies as high as 10 MeV (even though the spectra were truncated at 1 MeV for inclusion in SD-WACCM). A baseline simulation was also performed, which included auroral electrons but no MEE precipitation. Ionization rate comparisons show that the MP15 electron fluxes correspond to significantly more ionization than the CMIP6 fluxes during the 2003 SH winter. This is probably due to the utilization of both MEPED telescopes in the MP15 calculation, with some contribution from the different spectral fit used in the MP15 flux calculation, which would increase the flux of electrons on the high energy tail of the distribution.

Results from the three WACCM simulations were compared with observations from the MIPAS infrared emission spectrometer as well as from the HALOE, SAGE III, and POAM III solar occultation instruments. NO_x mixing ratios from the CMIP6 and MP15 simulations agree better with observations than NO_x mixing ratios from the baseline simulation. Compared to the CMIP6 simulation, the MP15 simulation shows significantly more EEP-NO_x descending into the stratosphere, which is in better overall agreement with observations. Particularly noteworthy is the substantially improved agreement in the MP15 simulation at mid-latitudes (40°S-50°S).

Although the MP15 simulation reproduces the main body of descending EEP-NO_x reasonably well, some significant disagreements with the observations are also apparent. For instance, NO_x mixing ratios at the lower altitude edge of the descending body of EEP-NO_x are underestimated in all three simulations relative to the MIPAS data. Comparisons between WACCM and MIPAS CO, a tracer of vertical motion, suggest that in the specified dynamics version of WACCM descent rates in the lower mesosphere and upper stratosphere are too low early in the winter, resulting in too little descending EEP-NO_x. On the other hand, the MIPAS comparisons suggest that there is too much EEP-NO_x above 70 km in late August in the MP15 simulation, leading to a high bias as the excess NO_x descends into the stratosphere; this is also

true for the CMIP6 simulation, but to a much smaller degree. This might indicate too much production of EEP-NO_x in the mesosphere and lower thermosphere; but it is also consistent with descent rates that are too strong in late winter, as suggested by the comparisons of modeled and measured values of CO. At mid-latitudes, all three models underestimated EPP-NO_x descending into the stratosphere. Additional ionization at energies > 1 MeV could be contributing to the lack of EEP-NO_x shown in the model simulations here. Future work will examine the contribution of HEE precipitation during geomagnetic activity.

To summarize, the WACCM simulation that includes MP15 electron fluxes reproduces the descent of EEP-NO_x from the mesosphere into the stratosphere during the 2003 SH winter more accurately than the simulation that includes the CMIP6 electron fluxes. The CMIP6 simulation performs better than the baseline simulation, but it underestimates ionization rates, resulting in less NO_x and OH production from EEP. Although not investigated in this study, underestimating NO_x and HO_x would also lead to underestimating ozone destruction. An updated version of the CMIP6 electron data set has been produced recently (*van de Kamp et al*., 2018), and should be included for future comparisons with other electron data sets. However, a key advantage of the MP15 data set over CMIP6 is that MP15 incorporates measurements from both the 0° and 90° MEPED telescopes. Thus the MP15 calculations include a wider range of precipitating electron pitch angles and energies. Another advantage is that the MP15 multi-function spectral fit used to convert the MEPED integrated channel data to differential fluxes better constrains the high-energy tail of the EEP distribution than a simple power law, as used in the CMIP6 calculations. The model-measurement comparisons in this study confirm that including both electron detector telescopes, which means considering the full range of pitch angles, is critical for accurate simulations of the effects of EEP on the atmosphere, particularly at mid-latitudes. This study confirms that a comprehensive understanding of the impacts of EEP on the atmosphere requires consideration of the full range of pitch angles of precipitating electrons, as well as the full range of energies, as first suggested more than three decades ago by *Baker et al*. (1987).

Figure Captions

Figure 1: Energetic electron ionization rates at 90 km (top) for 11 May 2003 from CMIP6 (a) and MP15 (b) and 75 km (bottom) for 2 May 2003 from CMIP6 (c) and MP15 (d).

Figure 2: Energetic electron ionization rates for 2003, averaged from 50°S - 80°S (top) and 30°S - 50°S (bottom), from CMIP6 (a, d) and MP15 (b, e). The ionization rate differences are shown in (c, f).

Figure 3: CMIP6 (a) and MP15 (b) model simulations minus the baseline simulation for OH mixing ratios averaged from 50°S-80°S. The black line indicates the MEE ionization at 0.01 hPa for the respective simulations.

Figure 4: NO_x mixing ratios averaged over latitudes from 70°S - 90°S, from MIPAS (a) and from the baseline (b), CMIP6 (c) and MP15 (d) WACCM simulations at the times and locations of the MIPAS measurements. The black lines denote the MIPAS 16 ppbv and 64 ppbv NO_x contours. White regions indicate missing MIPAS data or regions where MIPAS errors were >200%.

Figure 5. Differences between MIPAS and WACCM NO_x mixing ratios [100×(WACCM-MIPAS)/MIPAS] for the baseline (a), CMIP6 (b) and MP15 (c) simulations. All panels are averaged from 70°S - 90°S. Model results are taken at the MIPAS times and satellite locations.

Figure 6: NO_x mixing ratios averaged over 40°S - 50°S, from MIPAS (a) and from the baseline (b), CMIP6 (c) and MP15 (d) WACCM simulations at the times and locations of the MIPAS measurements. The dashed black line denotes the MIPAS 16 ppbv NO_x contour.

Figure 7: Comparisons of observations of NO_x at 45 km altitude from HALOE (top row), and NO_2 at 40 km from SAGE III (middle row) and POAM III (bottom row), with results from the baseline (left column), CMIP6 (middle) and MP15 (right) simulations at the corresponding measurement locations and times. HALOE plots show all individual measurements poleward of 40°S; POAM and SAGE plots show 7-day running means; measurement latitudes are shown in blue and referenced to the right axis.

Figure 8. CO mixing ratios from MIPAS (a) and baseline WACCM (b) and CO percent differences, 100*(WACCM-MIPAS)/MIPAS (c). Panels show averages from 70°S - 90°S during March-September 2003. Model results are taken at the MIPAS times and satellite locations. The black lines indicate the MIPAS 32 ppbv, 256 ppbv and 1024 ppbv CO contours for reference.

Acknowledgments

This research has been funded by the NASA Living With a Star program, grant NNX14AH54G, the NSF Frontiers of Earth System Dynamics program, grant AGS 1135432, and the NSF Coupling, Energetics and Dynamics of Atmospheric Regions, grant AGS 1651428. M. van de Kamp has been supported by the Academy of Finland project 276926 (SECTIC: Sun-Earth Connection Through Ion Chemistry). B. Funke acknowledges support by the Spanish MCINN (ESP2017-87143-R) and EC FEDER funds. We thank NCAR for the use of the WACCM model as well as their high-performance computing. The National Center for Atmospheric Research is

operated by the University Corporation for Atmospheric Research under sponsorship of the National Science Foundation. The CMIP6 dataset, as well as a metadata description and a number of tools to convert and implement the solar forcing data, can be found here: http://solarisheppa.geomar.de/cmip6.

References

Allen, D. R., et al. (1999). Observations of middle atmosphere CO from the UARS ISAMS during the early northern winter 1991/92. *Journal of Atmospheric Sci*ence, *56*, 563-583. http://doi.org/10.1175/1520-0469(1999)056<0563

Andersson, M. E., Verronen, P. T.,Marsh, D. R., Seppälä, A., Päivärinta, S.-M., Rodger, C. J., van de Kamp, M. (2018). Polar ozone response to energetic particle precipitation over decadal timescales: The role of medium-energy electrons. *Journal of Geophysical Research: Atmospheres, 123*, 607–622. https://doi.org/10.1002/2017JD027605

Andersson, M. E.,Verronen, P. T., Rodger, C. J., Clilverd, M. A., Seppälä, A. (2014). Missing driver in the Sun–Earth connection from energetic electron precipitation impacts mesospheric ozone. *Nature Communications*, *5*, 5197. https://doi.org/10.1038/ncomms6197

Asikainen, T., Mursula, K., and Maliniemi., V (2012). Correction of detector noise and recalibration of NOAA/MEPED energetic proton fluxes. *Journal of Geophysical Research, 117*, A09204. https://doi:10.1029/2012JA017593

Asikainen, T., and K. Mursula (2013). Correcting the NOAA/MEPED energetic electron fluxes for detector efficiency and proton contamination. *Journal of Geophysical Research Space Physics*, 118, 6500–6510. https://doi:10.1002/jgra.50584

Asikainen, T., and M. Ruopsa. (2019). New Homogeneous Composite Of Energetic Electron Fluxes From POES: 2. Intercalibration of SEM-1 and SEM-2, *Journal of Geophysical Research: Space Physics*, 124, 1203-1221. https://doi.org/10.1029/2018JA026214

Baker, D. N., J. B. Blake, D. J. Gorney, P. R. Higbie, R. W. Klebesadel, and J. H. King (1987). Highly relativistic magnetospheric electrons: A role in coupling to the middle atmosphere. *Geophysical Research Letters, 14*, 1027-1030.http://doi.org/10.1029/GL014i010p01027

Brakebusch, M., Randall C. E., Kinnison D. E., Tilmes S., Santee M. L., & Manney G. L. (2013). Evaluation of Whole Atmosphere Community Climate Model simulations of ozone during Arctic winter 2004–2005. *Journal of Geophysical Research: Atmospheres*, 118, 2673–2688. https://doi.org/10.1002/jgrd.50226

Clilverd, M. A., C. J. Rodger, R. J. Gamble, T. Ulich, T. Raita, A. Seppälä, J. C. Green, N. R. Thomson, J.-A. Sauvaud, and M. Parrot (2010). Ground-based estimates of outer radiation belt energetic electron precipitation fluxes into the atmosphere. *Journal of Geophysical Research Space Physics, 115*, A12304. http://doi.org/10.1029/2010JA015638

Clilverd, M. A., N. Cobbett, C. J. Rodger, J. B. Brundell, M. H. Denton, D. P. Hartley, J. V. Rodriguez, D. Danskin, T. Raita, and E. L. Spanswick (2013). Energetic electron precipitation characteristics observed from Antarctica during a flux dropout event. *Journal of Geophysical Research Space Physics, 118*, 6921–6935. http://doi.org/10.1002/2013JA019067

Codrescu, M., T. Fuller-Rowell, R. Roble, and D. Evans (1997). Medium energy particle precipitation influences on the mesosphere and lower thermosphere, *Journal of Geophysical. Research: Space Physics*, *102*(A9), 19977-19987

Crutzen, P. J., (1979). The Role of NO and NO_2 on the chemistry of the troposphere and stratosphere. Annual Review of Earth Planetary Science, 7, 443-472.

Evans, D. S., and M. S. Greer (2004). Polar orbiting environmental satellite space environment monitor-2: Instrument descriptions and archive data documentation. NOAA Tech. Mem. 1.4, Space Environ. Cent., Boulder, Colo.

Eyring, V., Arblaster J. M., Cionni I., Sedláček J., Perlwitz J., Young P. J., … Watanbe S. (2013). Long-term ozone changes and associated climate impacts in CMIP5 simulations. *Journal of Geophysical Research: Atmospheres*, 118, 5029–5060. https://doi.org/10.1002/jgrd.50316

Eyring, V., Bony, S., Meehl, G. A., Senior, C. A., Stevens, B., Stouffer, R.J., and Taylor, K. E. (2016). Overview of the Coupled Model Intercomparison Project Phase 6 (CMIP6) experimental design and organization. *Geosciences Model Development*., *9*, 1937-1958. https://doi.org/10.5194/gmd-9-1937-2016

Fang, X., Randall, C. E., Lummerzheim, D., Solomon, S. C., Mills, M. J., Marsh, D. R., … Lu, G. (2008).Electron impact ionization: A new parameterization for 100 eV to 1 MeV electrons. *Journal of Geophysical Research, 113,* A09311. https://doi.org/10.1029/2008JA013384

Fang, X., C. E. Randall, D. Lummerzheim, W. Wang, G. Lu, S. C. Solomon, and R. A. Frahm (2010). Parameterization of monoenergetic electron impact ionization. *Geophysical Research Letters*, *37*, L22106. http://doi.org/10.1029/2010GL045406

Fischer, H., et al. (2008). MIPAS: An instrument for atmospheric and climate research. *Atmospheric Chemistry and Physics,, 8*, 2151-2188

Funke, B., Baumgaertner A., Calisto M., Egorova T., Jackman C. H., Kieser J., … Wissing J. M. (2011). Composition changes after the "Halloween" solar proton event: the High Energy Particle Precipitation in the Atmosphere (HEPPA) model versus MIPAS data intercomparison study. *Atmospheric Chemistry and Physics, 11*, 9089-9139. https://doi.org/10.5194/acp-11-9089-2011

Funke, B., Puertas, M. L., Holt, L., Randall, C. E., Stiller, G. P., and von Clarmann, T., Hemispheric distributions and interannual variability of NOy produced by energetic particle precipitation in 2002–2012 (2014). *Journal of Geophysical Research,* 119, 13565–13582, doi:10.1002/2014JD022423

Gannon, J. L., X. Li, and D. Heynderickx (2007), Pitch angle distribution analysis of radiation belt electrons based on Combined Release and Radiation Effects Satellite Medium Electrons A data, J. Geophys. Res., 112, A05212, doi:10.1029/2005JA011565.

Gordley, L. L., et al. (1996). Validation of nitric oxide and nitrogen dioxide measurements made by the Halogen Occultation Experiment for UARS platform. *Journal of Geophysical Research*, **101**, 10,241–10,266, doi:10.1029/95JD02143

Green, J. C. (2013). MEPED Telescope Data Processing Algorithm Theoretical Basis Document. NOAA NGD

Gu, X., Z. Zhao, B. Ni, Y. Shprits, and C. Zhou (2011). Statistical analysis of pitch angle distribution of radiation belt energetic electrons near the geostationary orbit: CRRES observations. *Journal of Geophysical Research, 116,* A01208, doi:10.1029/2010JA016052

Harvey, V. L., C. E. Randall, and R. L. Collins (2015). Chemical definition of the mesospheric polar vortex. *Journal of Geophysical Research: Atmospheres, 120,* 10,166–10,179, http://doi.org/10.1002/2015JD023488

Hurrell, J. W., Holland M. M., Gents P. R., Ghan S., Kay J. E., Kushner P. J., … Marshall S. (2013). The Community Earth System Model: A framework for collaborative research. *Bulletin of the American Meteorological Society, 94,* 1339–1360. https://doi.org/10.1175/BAMS-D-12-00121.1

Jackman, C. H., Frederick J. E., & Stolarski, R.S. (1980). Production of Odd Nitrogen in the Stratosphere and Mesosphere: An Intercomparison of Source Strengths. *Journal of Geophysical Research: Atmospheres, 85,* 7495-7505. https://doi.org/10.1029/JC085iC12p07495

Jackman, C. H., Cerniglia, M. C., Nielsen, E. J., Allen, D. J., Zawodny, J. M., McPeters, R. D., … Rood, R. B. (1995). Two-dimensional and three-dimensional model simulations, measurements and interpretation of the influence of the October 1989 solar proton events on the middle atmosphere. *Journal of Geophysical Research: Atmospheres, 100,* 11641– 11660. https://doi.org/10.1029/95JD00369

Jackman, C. H. and McPeters, R. D. (2004). The Effect of Solar Proton Events on Ozone and Other Constituents, in: Solar Variability and its Effects on Climate. *Geophys. Mon. 141,* 305–319

Jackman, C. H., Marsh, D. R., Vitt, F. M., Garcia, R. R., Fleming, E. L., Labow, G. J., … Stiller, G. P. (2008). Short and medium-term atmospheric constituent effects of very large solar proton events. *Atmospheric Chemistry and Physics, 8,* 765-785. https://doi.org/10.5194/acp-8-765-2008

Jackman, C. H., Marsh, D. R., Vitt, F. M., Garcia, R. R., Randall, C. E., Fleming, E. L., & Frith, S. M. (2009). Long-term middle atmospheric influence of very large solar proton events. *Journal of Geophysical Research: Atmospheres, 114,* D11304. https://doi.org/10.1029/2008JD011415

Kinnison, D. E., Brasseur, G. P., Walters, S., Garcia, R. R., Marsh, D. R., Sassi, F., … Simmons, A. J. (2007). Sensitivity of chemical tracers to meteorological parameters in the MOZART-3 chemical transport model. *Journal of Geophysical Research: Atmospheres, 112,* D20302. https://doi.org/10.1029/2006JD007879

Lam, M. M., R. B. Horne, N. P. Meredith, S. A. Glauert, T. Moffat-Griffin, and J. C. Green (2010). Origin of energetic electron precipitation >30 keV into the atmosphere. *Journal of Geophysical Research: Space Physics, 115,* A00F08. http://doi.org10.1029/2009JA014619

Lamarque, J.-F., et al. (2012). CAM-chem: Description and evaluation of interactive atmospheric chemistry in the Community Earth System Model. *Geosciences Model Development, 5,* 369–411. http://doi.org/10.5194/gmd-5-369-2012

López-Puertas, M., Funke, B., Gil-Lopez, S., von Clarmann, T., Stiller, G. P., Höpfner, M., … Jackman, C. H. (2005). HNO3, N2O5, and ClONO2 enhancements after the October–November 2003 solar proton events. *Journal of Geophysical Research: Space Physics, 110,* A09S44. https://doi.org/10.1029/2005JA011051

Marsh, D.R., M.J. Mills, D.E. Kinnison, J. Lamarque, N. Calvo, and L.M. Polvani (2013). Climate Change from 1850 to 2005 Simulated in CESM1(WACCM). *Journal of Climate, 26*, 7372–7391. http://doi.org/10.1175/JCLI-D-12-00558.1

Matthes, K., Funke, B., Andersson, M. E., Barnard, L., Beer, J., Charbonneau, P., Clilverd, M. A., Dudok de Wit, T., Haberreiter, M., Hendry, A., Jackman, C. H., Kretzschmar, M., Kruschke, T., Kunze, M., Langematz, U., Marsh, D. R., Maycock, A. C., Misios, S., Rodger, C. J., Scaife, A. A., Seppälä, A., Shangguan, M., Sinnhuber, M., Tourpali, K., Usoskin, I., van de Kamp, M., Verronen, P. T., and Versick, S.: Solar forcing for CMIP6 (v3.2). *Geosciences Model Development 10*, 2247-2302. https://doi.org/10.5194/gmd-10-2247-2017, 2017

Moreno-Villanueva M., M. Wong, T. Lu, Y. Zhang, H. Wu (2017). Interplay of space radiation and microgravity in DNA damage and DNA damage response. *Nature*, *3*, 14. https://doi.org/10.1038/s41526-017-0019-7

Nesse Tyssøy, H., M. I. Sandanger, L.-K. G. Ødegaard, J. Stadsnes, & A. Aasnes1 A. E. (2016). Energetic Electron Precipitation into the Middle Atmosphere - Constructing the Loss Cone Fluxes from MEPED POES. *Journal of Geophysical Research: Space Physics, 121*, 5693-5707. http://doi.org/ 10.1002/2016JA022752

Newnham, D. A., Clilverd, M. A., Rodger, C. J., Hendrickx, K., Megner, L., Kavanagh, A. J., et al. (2018). Observations and modeling of increased nitric oxide in the Antarctic polar middle atmosphere associated with geomagnetic storm-driven energetic electron precipitation. *Journal of Geophysical Research: Space Physics, 123*, 6009–6025. https://doi.org/ 10.1029/2018JA025507

O'Brien, T. P., and S. K. Morley (2011). Documentation of C Inversion Library, from the *IRBEM* library, [Available at http://irbem.sourceforge.net/.]

Orsolini, Y., M. L. Santee, G. L. Manney, and C. E. Randall (2005), An upper stratospheric layer of enhanced HNO3 following exceptional solar storms. *Geophysical Research Letters, 32(12),* L12S01. http://doi.org/10.1029/2004/GL021588

Parsons J. L., and L.W. Townsend (2000). Interplanetary Crew Dose Rates for the August 1972 Solar Particle Event. *Radiation Research*, *153*, 729-733. https://doi.org/10.1667/0033-7587(2000)153[0729:ICDRFT]2.0.CO;2

Peck, E. D., Randall, C. E., Green, J. C., Rodriguez, J. V., & Rodger, C. J. (2015). POES MEPED differential flux retrievals and electron channel contamination correction. *Journal of Geophysical Research: Space Physics, 120*, 4596–4612. https://doi.org/10.1002/2014JA020817

Picone, J. M., Hedin, A.E., Drob, D.P., & Aikin, A.C. (2002). NRLMSISE-00 empirical model of the atmosphere: Statistical comparisons and scientific issues. *Journal of Geophysical Research*, 107(A12), 1468. https://doi:10.1029/2002JA009430, 2002

Randall, C. E., Harvey, V. L., Holt, L. A., Marsh, D. R., Kinnison, D., Funke, B., & Bernath, P. F. (2015). Simulation of energetic particle precipitation effects during the 2003–2004 Arctic winter. *Journal of Geophysical Research: Space Physics, 120*, 5035-5048. https://doi.org/10.1002/2015JA021196

Randall, C. E., V. L. Harvey, C. S. Singleton, S. M. Bailey, P. F. Bernath, M. Codrescu, H. Nakajima, and J. M. Russell III (2007). Energetic particle precipitation effects on the Southern Hemisphere stratosphere in 1992–2005. *Journal of Geophysical Research, 112*, D08308. http://doi.org/10.1029/2006JD007696

Randall, C. E., V. L. Harvey, C. S. Singleton, P. F. Bernath, C. D. Boone, and J. U. Kozyra (2006). Enhanced NO_x in 2006 linked to strong upper stratospheric Arctic vortex. *Geophysical Research Letters, 33*, L18811. http://doi.org/10.1029/2006GL027160

Randall, C. E., et al. (2002). Validation of POAM III NO_2 measurements. *Journal of Geophysical Research. 197*(D20), 4432. http://doi.org/10.1029/2001JD001520

Rault, D. F. (2004). Ozone, NO2 and aerosol retrieval from SAGE III limb scatter measurements, in Proc. SPIE 5571. *Remote Sensing of Clouds and the Atmosphere IX*, 205. http://doi.org/10.1117/12.564899

Rienecker M. M, Suarez, M. J., Gelaro, R., Todling, R., Bacmeister, J., Liu, E., … Woollen J. (2011). MERRA: NASA's modern-era retrospective analysis for research and applications. *Journal of Climate, 24*, 3624–3648. https://doi.org/10.1175/JCLI-D-11-00015.1

Roble, R. G., and Rees M. H., (1977). Time-dependent studies of the aurora: Effects of particle precipitation on the dynamic morphology of ionospheric and atmospheric properties. P*lanetary Space Sciences*, 22, 623-631.

Roble, R. G., and Ridley, E. C. (1987). An auroral model for the NCAR thermospheric general circulation model (TGCM). *Annales Geophysicae, 5A(6)*, 369-382

Rodger, C. J., M. A. Clilverd, J. C. Green, and M. M. Lam (2010a). Use of POES SEM-2 observations to examine radiation belt dynamics and energetic electron precipitation into the atmosphere. *Journal of Geophysical Research: Space Physics, 115*, A04202. http://doi.org/10.1029/2008JA014023

Rodger, C. J., A. J. Kavanagh, M. A. Clilverd, and S. R. Marple (2013). Comparison between POES energetic electron precipitation observations and riometer absorptions: Implications for determining true precipitation fluxes. *Journal of Geophysical Research: Space Physics*, 118, 7810–7821, doi:10.1002/2013JA019439

Russell, J. M. III, L. L. Gordley, J. H. Park, S. R. Drayson, W. D. Hesketh, R. J. Cicerone, A. F. Tuck, J. E. Frederick, J. E. Harries, and P. J. Crutzen (1993). The Halogen Occultation 152 Experiment. *Journal of Geophysical Research. 98*, 10,777-10,797

Seppälä, A., Douma, E., Rodger, C. J., Verronen, P. T., Clilverd, M. A., & Bortnik, J. (2018). Relativistic electron microburst events: Modeling the atmospheric impact. *Geophysical Research Letters, 45*, 1141–1147. https://doi.org/10.1002/2017GL075949

Smith-Johnsen, C., Marsh, D. R., Orsolini, Y., Nesse Tyssøy, H., Hendrickx, K., Sandanger, M. I., et al. (2018). Nitric oxide response to the April 2010 electron precipitation event: Using WACCM and WACCM-D with and without medium-energy electrons. *Journal of Geophysical Research: Space Physics, 123*, 5232–5245. https://doi.org/10.1029/2018JA025418

Solomon, S., Rusch, D. W., Gérard, J. C., Reid, G. C., & Crutzen, P. J. (1981). The effect of particle precipitation events on the neutral and ion chemistry of the middle atmosphere: II. Odd hydrogen. *Planetary and Space Science, 8*, 885–893. https://doi.org/10.1016/0032-0633(81)90078-7

Solomon, S., Crutzen, P. J, & Roble, R. G. (1982). Photochemical coupling between the thermosphere and the lower atmosphere: 1. Odd nitrogen from 50 to 120 km. *Journal of Geophysical Research: Oceans, 87(C9),* 7206–7220. https://doi.org/10.1029/JC087iC09p07206

Solomon, S., Kinnison, D., Bandoro, J., & Garcia, R. (2015). Simulation of polar ozone depletion: An update. *Journal of Geophysical Research: Atmospheres*, *120*, 7958–7974. https://doi.org/10.1002/2015JD023365

Thorne, R. M. (1980). The importance of energetic particle precipitation on the chemical composition of the middle atmosphere. *Pure and Applied Geophysics*, *118*, 128–151

Turner, D. L., Y. Y. Shprits, M. Hartinger, and V. Angelopoulos (2012b). Explaining sudden losses of relativistic electrons during geomagnetic storms. Nature Phys., 8, doi:10.1038/NPHYS2185.

Vampola, A. L. (1998), Outer zone energetic electron environment update, in Conference on the High Energy Radiation Background in Space, 128–136, IEEE Press, Piscataway, N. J.

van de Kamp, M., A. Seppälä, M. A. Clilverd, C. J. Rodger, P. T. Verronen, and I. C. Whittaker (2016). A model providing long-term data sets of energetic electron precipitation during geomagnetic storms. *Journal of Geophysical Research: Atmospheres*, *121*, 12,520–12,540. http://doi,org/10.1002/2015JD024212

Verronen, P. T., M. E. Andersson, A. Kero, C.-F. Enell, J. M. Wissing, E. R. Talaat, K. Kauristie, M. Palmroth, T. E. Sarris, and E. Armandillo (2015). Contribution of proton and electron precipitation to the observed electron concentration in October-November 2003 and September 2005. *Ann. Geophys.*, *33*, 381–394. http://doi.org/10.5194/angeo-33-381-2015

Verronen, P. T., M. E. Andersson, D. R. Marsh, T. Kovács, and J. M. C. Plane (2016). WACCM-D—Whole Atmosphere Community Climate Model with D-region ion chemistry. *J. Adv. Model. Earth Syst.*, *8*, 954–975. http://doi.org/10.1002/2015MS000592

Vitt, F. M., & Jackman C. H. (1995). A Comparison of Sources of Odd Nitrogen Production from 1974 through 1993 in the Earth's Atmosphere as Calculated Using a Two-Dimensional Model. *Journal of Geophysical Research: Atmospheres*, *101*, 6729-6739. https://doi.org/10.1029/95JD03386

Yando, K., R. M. Millan, J. C. Green, and D. S. Evans (2011). A Monte Carlo simulation of the NOAA POES Medium Energy Proton and Electron Detector instrument. *J. Geophys. Res.*, *116*, A10231. http://doi.org/10.1029/2011JA016671